arXiv:1604.07479v2 [math.NA] 20 Dec 2016

EXPLICIT LEAST-DEGREE BOUNDARY FILTERS FOR DISCONTINUOUS GALERKIN*

DANG-MANH NGUYEN† AND JÖRG PETERS†

Abstract. Convolving the output of Discontinuous Galerkin (DG) computations using spline filters can improve both smoothness and accuracy of the output. At domain boundaries, these filters have to be one-sided for non-periodic boundary conditions. Recently, position-dependent smoothness-increasing accuracy-preserving (PSIAC) filters were shown to be a superset of the top-of-the-line one-sided RLKV and SRV filters. Since PSIAC filters can be formulated symbolically, convolution with PSIAC filters reduces to a sequences of small inner products with local DG output and hence provides a more stable and efficient implementation.

The paper focuses on the remarkable fact that, for the canonical hyperbolic test equation, new piecewise constant PSIAC filters of small support outperform the top-of-the-line boundary filters in the literature. Numerical experiments show that these least-degree filters reduce the error at the boundaries to less than the error even of the symmetric filters of the same support that are applied in the interior. Due to their simplicity, and since this least degree filter has an exact symbolic form, convolution is stable as well as efficient; and derivatives of the convolved output are easy to compute.

Key words. Discontinuous Galerkin; spline filter; shifted convolution; SIAC filtering; boundary filter; symbolic representation

AMS subject classifications. 65M12; 65D07

1. Introduction.

The output of Discontinuous Galerkin (DG) computations often captures higher order moments of the true solution [ML78]. Therefore post-processing DG output by convolution with splines can improve both smoothness and accuracy [BS77, CLSS03, JVSRV14]. In the interior of the domain of computation, symmetric smoothness increasing accuracy conserving (SIAC) spline filters have been demonstrated to provide optimal accuracy [CLSS03]. Near boundaries of the computational domain such symmetric filters need to be complemented by one-sided filters to accomodate non-periodic boundary data. The point-wise error and stability, of the pioneering Ryan-Shu boundary filters [RS03] have been noticeably improved upon, during the last decade [SRV11, MRK12, RLKV15, LRKV16].

Most recently these boundary filters have been simplified and improved by replacing numerical approximation with symbolic formulas, both in the uniform symmetric case [MRK15] and in the general case [Pet15]. For general knot sequences, [NP16] introduced a factored symbolic characterization of spline filters that facilitates their knots being shifted or scaled. This allowed characterizing the existing boundary filters as position-dependent SIAC spline filters (PSIAC filters). PSIAC coefficients are polynomial expressions in the position and the coefficients of these polynomial expressions are rational numbers for rational knot sequences. In the *boundary region*, where PSIAC filtering is deployed, PSIAC filtering converts the DG output to a single polynomial [NP16, Theorem 4.2]. The PSIAC filters can be symbolically precomputed for prototype filters and these prototype filters are easily scaled and shifted for a specific data set. The PSIAC characterization therefore replaces Gauss quadrature that is otherwise required to repeatedly derive, at each point near the boundary, a position-dependent filter to apply the filter to the DG output. PSIAC filtering then reduces to a sequence of single dot products between the filter vector and the short vectors

*This work was supported in part by NSF grant CCF-1117695 and NIH grant R01 LM011300-01

†Department of Computer & Information Science & Engineering, University of Florida. (nguyendm@ufl.edu, jorg@cise.ufl.edu).

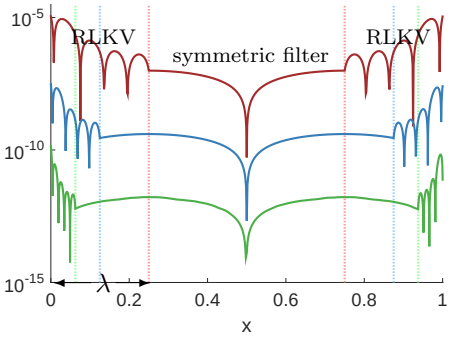

(a) Error filtered by RLKV in the boundary region

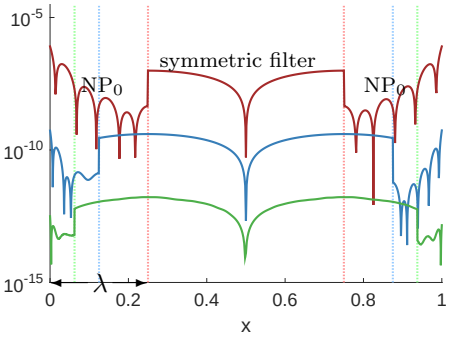

(b) Error filtered by NP_0 in the boundary region

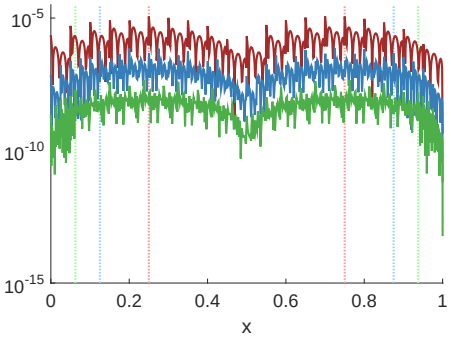

(c) DG error at final time $T = 1$

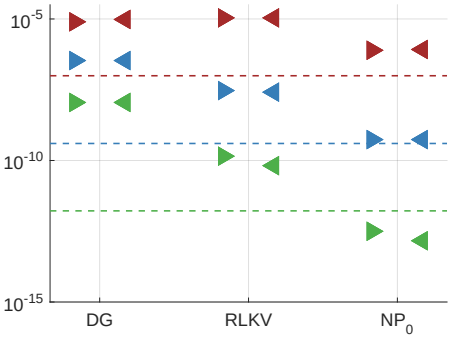

(d) Maximal errors restricted to the left $\triangleright$ and right $\triangleleft$ boundary region

FIG. 1. *Pointwise errors of the canonical partial differential equation* $u_\tau + u_x = 0$ (2.2) *at time* $\tau = 1$ *based on* $d = 3$ *DG output. Each subfigure shows top-most the mesh-size* $h = 20^{-1}$ *graph (red),* $h = 40^{-1}$ *(blue) and* $h = 80^{-1}$ *(green) at the bottom. (a,b) The interior, bordered by vertical dotted lines of the mesh-size color, is post-processed by the symmetric SIAC filter. The graph for the interior is therefore identical in (a) and (b). To the left of the left line is the* left boundary region $[0..\lambda]$ *and to the right of right line is the right boundary region. (a) Errors after convolving the data of the boundary regions with the one-sided RLKV filters [RLKV15] and the interior with the symmetric SIAC filter. This graph is identical to [RLKV15, Figure 5,top-right] (but is computed with the more new stabler symbolic formulation). (b) Errors after convolving the data of the boundary regions with the new least-degree PSIAC filters* NP_0*. (c) Errors of the degree* $d = 3$ *DG output. (d) The error in the left boundary region of (a) and (b) is indicated by* $\triangleright$ *and in the right by* $\triangleleft$*. The error of the symmetric SIAC filter applied in the interior is indicated by* $--$*. The error of the new PSIAC filter* NP_0 *is lower or on par with the optimally superconvergent symmetric SIAC filter in the interior.*

of local DG output. Finally, instead of approximating derivatives of the filtered DG output [Tho77, RSA05, RC09, LRKV16], derivatives of the PSIAC-filtered output have an explicit expression.

This paper introduces a new piecewise constant PSIAC filter, that we will refer to as the NP_0 filter. The simple NP_0 kernel outperforms both the superconvergent, but large-support and numerically unstable SRV boundary filter [SRV11] and the small-support and stable but suboptimal RLKV filter [RLKV15]. Here unstable means that SRV requires, for reliable results for cubic or higher DG order, quadruple precision.

[RLKV15]). To illustrate this point, Fig. 1 shows results for the canonical hyperbolic equation $u_\tau + u_x = 0$ (c.f. Eq. (2.2)). For three different mesh spacings the RLKV error near the boundaries exceeds the error of the symmetric SIAC filter that applies (only) in the interior. For large mesh spacing, the RLKV error in Fig. 1a even exceeds that of the unfiltered DG error in Fig. 1c. By contrast, Fig. 1b shows that the new PSIAC filter NP_0 to always reduce the DG error on the boundary, even below the error of the symmetric SIAC filter. This message is condensed in Fig. 1d. Here the maximal error of the symmetric SIAC filter of degree d in the interior is displayed as dashed lines and the error near the left and right boundary by $\triangleright$, respectively $\triangleleft$. In fact, with d the polynomial degree of the DG output and k the degree of the spline filters, the theory of [JVSRV14] only guarantees a convergence order of $d+1+k$. Yet, extensive numerical experiments, presented in detail in the Appendix, for the canonical hyperbolic equation $u_\tau + u_x = 0$ for increasing final times T of the DG computation show the NP_0 filter with $k=0$ yielding optimal convergence of order $2d+1$. (The present paper does not aim to provide a formal investigation of optimal superconvergence of the NP_0 filter.)

Not only does the new NP_0 filter reduce the error, but, being piecewise constant, computing the convolution with the data is simple and stable. Leveraging the symbolic formula provided by [NP16], filtering the DG output at an endpoint, say $x=0$, amounts to the scalar product of the local DG coefficient vector with a vector of the form (Eq. (2.11) of Theorem 2.5 in this paper):

$$\boldsymbol{\mathcal{V}} = Q_\lambda \boldsymbol{\lambda} \in \mathbb{Q}^{(3d+1)(d+1)}, \quad \boldsymbol{\lambda} := \left[\lambda^0 \cdots \lambda^r\right]^t \tag{1.1}$$

where $[0..\lambda]$ is the left boundary region and Q_λ is a matrix with rational entries. Q_λ depends only on the space of polynomials used for the DG approximation and on the space of filter kernels, see Eq. (2.11). In practice, the local DG coefficient vector is multiplied with the matrix Q_λ in advance yielding a vector of size $3d+1$ to be multiplied with $\boldsymbol{\lambda}$.

To demonstrate the simplicity of the new NP_0 filter, we contrast the entries with the largest absolute values, the central four entries of $\boldsymbol{\mathcal{V}}$, both for the NP_0 filter and the SRV filter (rederived in its more stable PSIAC form) when $d=3$:

$$\begin{aligned}\boldsymbol{\mathcal{V}}_4(\mathrm{NP}_0) &= 10080^{-1}\left[70381 \quad 70381 \quad -56627 \quad -56627\right]\\ \boldsymbol{\mathcal{V}}_4(\mathrm{SRV}) &= 15256200960000^{-1}\big[3549982809648204 \quad 9809076669570393\\ &\qquad\qquad 11473452075703833 \quad 6592494198365004\big].\end{aligned} \tag{1.2}$$

While the entries of $\boldsymbol{\mathcal{V}}$ for the new filters are fractions of integers with 5 digits at most, those alternating numbers for the SRV filters have up to 17 digits. Crucially, as shown in Fig. 2, the fractions for the new NP_0 filter are also much smaller. For example, Fig. 2 shows that for $d=3$ the alternating coefficients of the SRV filter are two orders of magnitude larger than those of the NP_0 filter.

In summary,

- $\triangleright$ the PSIAC boundary filter NP_0 is simple and explicit; and
- $\triangleright$ numerical experiments in double floating point precision on the canonical wave equation show NP_0 to have a convergence rate of $2d+1$ where d is the piecewise degree of the DG output.

Organization. Section 2 introduces notation, spline convolution and the canonical test equations. followed by a review of the literature in more detail. Section 3 focuses

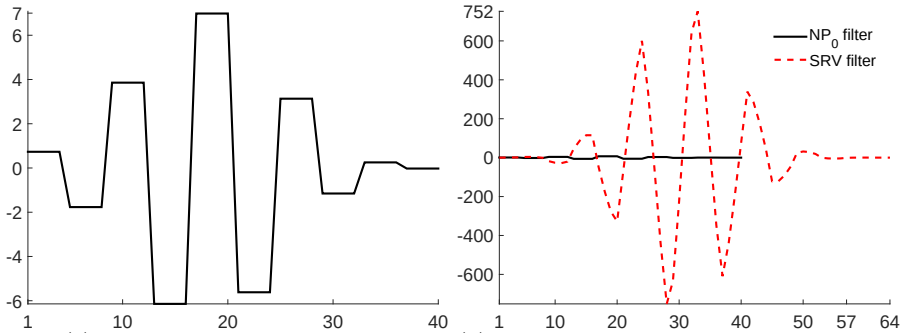

(a) Coefficients of new NP_0 filter (b) Coefficients of SRV filter vs. of NP_0 filter

FIG. 2. *Size of the entries of* $\boldsymbol{\nu} = Q_\lambda \boldsymbol{\lambda}$ *for filtering* $d = 3$ *DG output at a boundary point* $x = 0$. *Note the 100-fold difference in scale between (a) and (b).*

on the new NP_0 filter and compares it to the existing SRV and RLKV filters in their improved symbolic PSIAC form. Section 4 compares the SRV, RLKV, NP_0 and the symmetric SIAC filters numerically on three variants of the canonical hyperbolic equation.

2. Notation and Definitions. This section establishes the notation for filters and DG output, exhibits the canonical test problem, the DG method, and reproducing filters and reviews one-sided and position-dependent SIAC filters in the literature.

We denote by $f * g$ the convolution of a function f with a function g, i.e.

$$(f * g)(x) := \int_{\mathbb{R}} f(t)\, g(x-t)\, \mathrm{d}t = (g * f)(x),$$

for every x where the integral exists. Filtering means convolving a function f with a kernel g.

2.1. Sequences, Splines, and Reproduction. The goal of *SIAC filtering* is to spatially smooth out the DG output $u(x,\tau)$ by convolution in x with a linear combination of B-splines. Typically filtering is applied after the last time step when $\tau = T$. Specifically, we will focus on piecewise polynomial SIAC spline kernels $f : \mathbb{R} \to \mathbb{R}$ such that convolution of f with monomials $(\cdot)^\delta$ reproduces the monomials up to degree r. Let $\mathcal{J} := (0, \ldots, j_r)$ be a sequence of strictly increasing integers between 0 and j_r, abbreviate the sequences of consecutive integers as

$$i : j \;:=\; \begin{cases} (i, i+1, \ldots, j-1, j), \text{if } i \le j, \\ (i, i-1, \ldots, j+1, j), \text{if } i > j, \end{cases} \qquad s_{i:j} := (s_i, \ldots, s_j).$$

Let $B(x|t_{j:j+k+1})$ denote the unit integral B-spline with (non-decreasing) knot sequence $t_{j:j+k+1}$ (see [dB02]) related to the recursively defined B-spline $N(t \,|\, t_{i:i+k+1})$ by $N(t \,|\, t_{i:i+k+1}) = \frac{t_{i+k+1} - t_i}{k+1} B(t \,|\, t_{i:i+k+1})$. Then a *SIAC spline kernel of degree* k *and reproduction degree* r *with index sequence* $\mathcal{J}$ *and knot sequence* $t_{0:n}$ is a spline

$$f(x) := \sum_{j \in \mathcal{J}} f_j B(x|t_{j:j+k+1}),$$

of degree k with coefficients f_j chosen so that

$$\Big(\sum_{j\in\mathcal{J}} f_j B(\cdot|t_{j:j+k+1}) * (-\cdot)^\delta\Big)(x) = (-x)^\delta, \qquad \delta = 0:r. \tag{2.1}$$

We reserve the following symbols:

d	degree of the DG output;
m	number of intervals of the DG output;
$s_{0:m}$	*prototype* increasing break point sequence, typically integers; the break sequence of the DG output is $hs_{0:m}$;
k	degree of the filter kernel;
$r+1$	number of filter coefficients for reproduction of polynomials up to degree r;
$\mathcal{J} := (0,\ldots,j_r)$	index sequence; if the B-splines of the filter are consecutive, then $j_r = r$;
n	number of knot intervals spanned by the filter; $n = j_r + k + 1$;
$\mathbf{t} := t_{0:n}$	prototype (integer) knot sequence of the filter; the input knot sequence of the filter is $ht_{0:n} + \xi$ where ξ is the shift and h scales.

This notation is illustrated by the following example.

Example 2.1. *A linear DG output sequence on 200 uniform segments of the interval* $[-1..1]$ *implies* $d = 1$, $m = 200$, $h = \frac{1}{100}$ *and* $s_{0:m} = -100:100$. *A degree-one spline filter defined over the knot sequence* $\mathbf{t} := 0:6$ *and associated with the index set* $\mathcal{J} := \{0,3,4\}$ *corresponds to* $k = 1$, $n = 6$, $r = 2$ *and* $j_r = 4$. *The two B-splines defined over the knot sequences* $1:3$ *and* $2:4$ *are skipped.*

2.2. The canonical test problem and the Discontinuous Galerkin method. To demonstrate the performance of the filters on a concrete example, [RS03] used the following univariate hyperbolic partial differential wave equation:

$$\begin{aligned} \frac{du}{d\tau} + \frac{d}{dx}\Big(\kappa(x,\tau)\,u\Big) &= \rho(x,\tau), & x \in (a..b), \tau \in (0..T) \\ u(x,0) &= u_0(x), & x \in [a..b] \end{aligned} \tag{2.2}$$

subject to periodic boundary conditions, $u(a,\tau) = u(b,\tau)$, or Dirichlet boundary conditions $u(e,\tau) = u_0(\tau)$ where, depending on the sign of $\kappa(x,\tau)$, e is either a or b. Subsequent work [RS03, SRV11, RLKV15] adopted the same differential equation to test their new one-sided filters and to compare to the earlier work. Eq. (2.2) is therefore considered the *canonical test problem*. We note, however, that SIAC filters apply more widely, for example to FEM and elliptic equations [BS77].

In the DG method, the domain $[a..b]$ is partitioned into intervals by a sequence $hs_{0:m}$ of break points $a =: hs_0, \ldots, hs_m := b$. Assuming that the sequence is rational, scaling by h will later allow us to consider a prototype sequence $s_{0:m}$ of integers. Let $\mathbb{P}_h^d$ be the linear space of all piecewise polynomials with break points $hs_{0:m}$ and of degree less than or equal to d. We use modal or nodal scalar-valued basis functions $\phi_i(.\,;hs_{0:m})$ $0 \le i \le m$ of $\mathbb{P}_h^d$ that are linearly independent and satisfy the scaling relations

$$\phi_i(hx\,;hs_{0:m}) = \phi_i(x\,;s_{0:m}). \tag{2.3}$$

Relation (2.3) is typically used for refinement in FEM, DG or Iso-parametric PDE solvers. Examples of basis functions ϕ_i are Bernstein-Bézier basis functions [dB05], Lagrange polynomials dependent on Legendre-Gauss-Lobatto quadrature points [HW07], and Legendre polynomials.

The DG method approximates the time-dependent solution of Eq. (2.2) by

$$u(x,\tau) := \sum_{i=0}^{m} u_i(\tau)\,\phi_i(x\,;\,hs_{0:m}), \quad \phi_i \in \mathbb{P}_h^d. \tag{2.4}$$

Multiplying the two sides of Eq. (2.4) with a test function v and integrating by parts yields the weak form of Eq. (2.2):

$$\int_a^b \big(\frac{du}{d\tau}\,v - \kappa(x,\tau)u\,\frac{dv}{dx}\big)\,\mathrm{d}x = \int_a^b \rho(x,\tau)\,v\,\mathrm{d}x - \Big(\kappa(x,\tau)u(x,\tau)v(x)\Big)\Big|_{x=a}^{x=b}. \tag{2.5}$$

Substituting u on the left of Eq. (2.5) by (2.4), treating the rightmost, non-integral term of Eq. (2.5) as a numerical flux, and choosing $v(x) := \phi_j(x\,;\,hs_{0:m})$, yields a system of ordinary differential equations in τ with the coefficients $u_i(\tau)$, $0 \le i \le m$, as unknowns. This system can be solved by, e.g., a standard fourth-order four stage explicit Runge-Kutta method (ERK) [HW07, Section 3.4].

2.3. A synopsis of DG filtering. Since convolution with a symmetric SIAC kernel of a function g at x requires g to be defined in a two-sided neighborhood of x, near boundaries, Ryan and Shu [RS03] proposed convolving the DG output with a kernel whose support is shifted to one side of the origin: for x near the left domain endpoint a, the one-sided SIAC kernel is defined over $(x-a)+h\big(-(3d+1), -3d, \ldots, 0\big)$ where d is the degree of the DG output. The Ryan-Shu x-position-dependent one-sided kernel yields optimal L^2-convergence, but its point-wise error near a can be larger than that of the DG output.

In [SRV11], Slingerland-Ryan-Vuik improved the one-sided kernel by increasing its monomial reproduction from degree $r = 2d$ to degree $r = 4d$. This one-sided kernel reduces the boundary error when $d = 1$ but the kernel support is increased by $2d$ additional knot intervals and numerical roundoff requires quadruple precision calculations to determine the kernel's coefficients. ([SRV11] additionally required quadruple precision for computing the DG output.) Indeed, the coefficients of the boundary filters [RS03, SRV11, MRK12, RLKV15, MRK15] are computed by inverting a matrix whose entries are determined by Gaussian quadrature; and, as pointed out in [RLKV15], SRV filter matrices are close to singular.

Ryan-Li-Kirby-Vuik [RLKV15] therefore suggested an alternative one-sided position-dependent kernel that has the same support size as the symmetric kernel and has reproduction degree higher by one, enriching the spline space by one B-spline. This RLKV kernel is stably computed, as has been verified numerically, in double precision, up to input data degree $d = 4$ and joins the symmetric SIAC filter, applied in the interior, without a jump in error. However, the error of the RLKV kernel at the boundaries can be higher than that of the symmetric kernel and the L^2 and L^∞ superconvergence rates are sub-optimal [RLKV15] (c.f. Fig. 10,11,12). [LRKV16] additionally states that RLKV has a poorer derivative approximation than SRV filters.

[NP16] reinterprets the published one-sided filters in an explicit, symbolic form as position-dependent PSIAC spline filters. Symbolic expression of coefficients for spline filters have recently been developed in [MRK15] for uniform knot sequences and in [Pet15] for general knot sequences. Reinterpretation of the published filters in symbolic form improves their numerical stability.

2.4. Symbolic formulation of the filters. We split the DG data at any known discontinuities and treat the domains separately. Then convolution can be applied throughout a given closed interval $[a..b]$. A SIAC spline kernel with knot sequence $t_{0:r+k+1}$ is *symmetric* (about the origin in $\mathbb{R}$) if $t_\ell + t_{r+k+1-\ell} = 0$ for $\ell = 0 : \lceil (r+k+1)/2 \rceil$. Note that, unlike the (position-independent) classical symmetric SIAC filter, the position-dependent boundary kernel coefficients have to be determined afresh for each point x.

LEMMA 2.1 (SIAC coefficients [NP16]). *The vector* $\mathbf{f} := [f_0, \dots, f_r]^t \in \mathbb{R}^{r+1}$ *of B-spline coefficients of the SIAC filter with index sequence* $\mathcal{J} := (0, \dots, j_r)$ *and knot sequence* $t_{0:n}$ *is*

$$\mathbf{f} := \textit{first column of } M^{-1}, \quad M := M_{t_{0:n},\mathcal{J}} = \left[\sum_{|\boldsymbol{\omega}|=\delta} t_{j:j+k+1}^{\boldsymbol{\omega}} \right]_{\delta=0:r,\, j\in\mathcal{J}} \tag{2.6}$$

$$\textit{where} \quad t_{0:p}^{\boldsymbol{\omega}} := t_0^{\omega_0} \dots t_p^{\omega_p} \quad \textit{and} \quad |t_{0:p}| := \sum_{j=0}^{p} |t_j|$$

This characterization yields the following formula for the filter coefficients.

THEOREM 2.2 (Scaled and shifted SIAC coefficients are polynomial [NP16]). *The SIAC filter coefficients* $f_{\xi;\ell}$ *associated with the knot sequence* $ht_{0:n} + \xi$ *are polynomials of degree* r *in* ξ*:*

$$\mathbf{f}_\xi := [f_{\xi;\ell}]_{\ell=0:r} = \; M^{-1}_{t_{0:n},\mathcal{J}} \operatorname{diag}\Big(\Big[(-1)^\ell \binom{\ell+k+1}{\ell} \Big]_{\ell=0:r} \Big) \Big[\Big(\frac{\xi}{h}\Big)^{0:r} \Big]^t. \tag{2.7}$$

The following corollary implies that the kernel coefficients $f_{\xi;\ell}$, can be pre-computed stably, as scaled integers.

COROLLARY 2.3 (Coefficient polynomials $f_{\xi,\ell}$ have rational coefficients [NP16]). *If the knots* $t_{0:n}$ *are rational, then the filter coefficients* $f_{\xi,\ell}$ *are polynomials in* ξ *and* h *with rational coefficients.*

We can now define the PSIAC kernel.

DEFINITION 2.4 (PSIAC kernel). *A PSIAC kernel with index sequence* $\mathcal{J} = (0, \dots, j_r)$ *and knot sequence* $ht_{0:n} + x$ *has the form*

$$f_x(s) := \sum_{j\in\mathcal{J}} f_{x;j} B(s \,|\, ht_{j:j+k+1} + x), \quad s \in h[t_0, t_n] + x. \tag{2.8}$$

The DG output is convolved with a PSIAC kernel $f_{x-h\lambda}(s)$ of reproduction degree r, associated with an index sequence $\mathcal{J}$ and defined over shifted knots $ht_{0:n} + x - h\lambda$ – where the constant $h\lambda$ adjusts the filter kernel to the left or right boundary. Example 2.2 illustrates the simple explicit form of the PSIAC coefficients according to Theorem 2.2 and verifies that the corresponding PSIAC filter reproduces as predicted by the derivation.

EXAMPLE 2.2 (Reproduction by PSIAC filtering). *Let* $h = 1$*,* $k = 0$ *and* f_x *be the least degree PSIAC filter with* $t_{0:n} = \{-2, -1, 0\}$*,* $r = 1$*,* $\mathcal{J} = (0, 1)$*. According to* (2.8) *of Definition 2.4:*

$$\begin{aligned} f_x(s) :&= f_{x;0} B(s \,|\, \{-2,-1\} + x) + f_{x;1} B(s \,|\, \{-1,0\} + x) \\ &= f_{x;0}\, \chi_{[-2,-1]+x} + f_{x;1}\, \chi_{[-1,0]+x}, \qquad \chi_{[\alpha,\beta]}(s) := \begin{cases} 1, & \textit{if } s \in [\alpha,\beta]; \\ 0, & \textit{else} \end{cases} \end{aligned} \tag{2.9}$$

where $\chi_{[\alpha,\beta]}$ denotes the indicator function of the domain $[\alpha,\beta]$. Equation (2.7) *of Theorem 2.2 provides the formula*

$$\begin{bmatrix} f_{x;0} \\ f_{x;1} \end{bmatrix} := \begin{bmatrix} 1 & 1 \\ -2-1 & -1+0 \end{bmatrix}^{-1} \begin{bmatrix} 1 & 0 \\ 0 & -2 \end{bmatrix} \begin{bmatrix} 1 \\ x \end{bmatrix} = \frac{1}{2} \begin{bmatrix} 2x-1 \\ 3-2x \end{bmatrix}. \tag{2.10}$$

This choice of filter coefficients $f_{x;0}$ and $f_{x;1}$ satisfies Eq. (2.1). For $\delta = 0$:

$$(f_x * 1)(x) = \int_{\mathbb{R}} f_x(s)\mathrm{d}s = f_{x;0} \int_{\mathbb{R}} \chi_{[-2,-1]+x}(s)\,\mathrm{d}s + f_{x;1} \int_{\mathbb{R}} \chi_{[-1,0]+x}(s)\,\mathrm{d}s = 1.$$

For $\delta = 1$:
$$\begin{aligned}
(f_x * (-\cdot))(x) &= \int_{\mathbb{R}} f_x(s)\,(s-x)\,\mathrm{d}s \\
&= f_{x;0} \int_{\mathbb{R}} \chi_{[-2,-1]+x}(s)\,(s-x)\,\mathrm{d}s + f_{x;1} \int_{\mathbb{R}} \chi_{[-1,0]+x}(s)\,(s-x)\,\mathrm{d}s \\
&= f_{x;0} \int_{-2+x}^{-1+x} (s-x)\mathrm{d}s + f_{x;1} \int_{-1+x}^{0+x} (s-x)\mathrm{d}s \\
&= f_{x;0} \left(\frac{s^2}{2}\Big|_{s=-2+x}^{s=-1+x} - x \right) + f_{x;1} \left(\frac{s^2}{2}\Big|_{s=-1+x}^{s=0+x} - x \right) \\
&= f_{x;0}(-f_{x;1} - x) + f_{x;1}(f_{x;0} - x) = -x.
\end{aligned}$$

Leveraging Theorem 2.2, we can efficiently compute the convolution as follows.

THEOREM 2.5 (Efficient PSIAC filtering of DG output [NP16]). *Let $f_x(s)$ be a PSIAC kernel of reproduction degree r with index sequence $\mathcal{J} = (0,\ldots,j_r)$ and knot sequence $ht_{0:n} + x - h\lambda$. Let $u(x,\tau) := \sum_{i=0}^{m} u_i(\tau)\,\phi_i(x\,;\,hs_{0:m})$, $x \in [a,b]$ and $\tau \geq 0$, be the DG output. Let $\mathcal{I}$ be the set of indices of basis functions $\phi_i(.\,;\,hs_{0:m})$ with support overlapping $h[\lambda - t_n, \lambda - t_0]$. Then the* filtered DG approximation *is a polynomial in x of degree r:*

$$\big(u * f_x\big)(x) = \mathbf{u}_{\mathcal{I}}\, Q_\lambda \left[\big(\frac{x}{h} - \lambda\big)^{0:r} \right]^t. \tag{2.11}$$

$$\begin{aligned}
\mathbf{u}_{\mathcal{I}} &:= \big[u_i(\tau)\big]_{i\in\mathcal{I}}, \\
Q_\lambda &:= G_\lambda\, A\, M_{0,\mathbf{t},\mathcal{J}}^{-1}\ \mathrm{diag}(\big[(-1)^\ell \tbinom{\ell+k+1}{\ell}\big]_{\ell=0:r}), \\
G_\lambda &:= \left[\int_{\lambda-t_n}^{\lambda-t_0} \phi_i(s\,;\,s_{0:m})\, B(s \,|\, \lambda - t_{n-j:j_r-j})\,\mathrm{d}s \right]_{i\in\mathcal{I},\, j\in\mathcal{J}}.
\end{aligned} \tag{2.12}$$

A is the reversal matrix with 1 on the antidiagonal and zero else.

The factored representation implies that instead of recomputing the filter coefficients afresh for each point x of the convolved output as was the practice prior to [NP16], we simply pre-compute the coefficients corresponding to one prototype knot sequence $\mathbf{t}$ and, at runtime, pre-multiply with the data and post-multiply with the vector of shifted monomials scaled by h according to Eq. (2.11).

Increased multiplicity of an inner knot of the symmetric, position-independent SIAC kernel reduces its smoothness, and this, in turn, reduces the smoothness of the filtered output. By contrast, Theorem 2.5 shows that when the PSIAC knots are shifted along evaluation points x then PSIAC convolution yields a *polynomial*, i.e. the

representation near the boundary is infinitely smooth regardless of the knot multiplicity. *That is, we may view position-dependent filtering as a form of polynomial approximation.* For example, the RLKV-filtered output is a single polynomial over the boundary region where it applies.

EXAMPLE 2.3 (Coefficients of the RLKV-filtered DG output polynomial). *Let $d = k = 3$. Consider the canonical partial differential equation $u_\tau + u_x = 0$ of (2.2) for $x \in [0, 1]$ at final time $T = 1$ for mesh-sizes $h_i := 2^{-i}/10$, $i = 1, 2, 3$. The analytical solution of this equation is $u_e(x) = \sin 2\pi(x - T)$. Let $\lambda_{L,i} := 5h_i$, $\lambda_{R,i} := 1 - 5h_i$ and $f_{L,i,x}$ be the RLKV filters with respect to the left boundary regions. Applying the RLKV-filter to the DG output u_{h_i} computed for mesh size h_i yields a polynomial in x as predicted by Theorem 2.5:*

$$P_{L,i}(x) := (f_{L,i,x} * u_{h_i})(x) = \sum_{k=0}^{7} a_{k,i}(x - \lambda_{L,i})^k, \qquad x \in [0, \lambda_{L,i}], \tag{2.13}$$

where

$$\begin{bmatrix} a_{0,1} & \cdots & a_{3,1} \\ a_{4,1} & \cdots & a_{7,1} \end{bmatrix} = \begin{bmatrix} 0.999999901374753 & 0.000021494468508 & -19.738996791744032 & -0.008053345774016 \\ 64.88630724285224 & 0.623484670536888 & -82.011046997856752 & -11.875898409510508 \end{bmatrix}$$
$$\begin{bmatrix} a_{0,2} & \cdots & a_{3,2} \\ a_{4,2} & \cdots & a_{7,2} \end{bmatrix} = \begin{bmatrix} 0.707106780904271 & 4.442883051171333 & -13.95772600673645 & -29.233165736223864 \\ 45.9166940244231 & 57.754323004960845 & -59.8089096658096 & -57.790782092166637 \end{bmatrix}$$
$$\begin{bmatrix} a_{0,3} & \cdots & a_{3,3} \\ a_{4,3} & \cdots & a_{7,3} \end{bmatrix} = \begin{bmatrix} 0.382683432364482 & 5.804906304724222 & -7.553868156289703 & -38.194755175826380 \\ 24.85114895244633 & 75.39658368210462 & -32.618972790201198 & -71.729391408995241 \end{bmatrix}.$$

Analogously, by symmetry, the filtered data of the right boundary region is

$$P_{R,i}(x) := (f_{R,i,x} * u_{h_i})(x) = \sum_{k=0}^{7} (-1)^{k+1} a_{k,i}(x - \lambda_{R,i})^k, \quad x \in [\lambda_{R,i}, 1].$$

Fig. 3a plots the polynomials $P_{L,i}$ and $P_{R,i}$, the diffference between the polynomials and the exact solution (note the scale 10^{-5} in Fig. 3b) and the error in log scale Fig. 3c. Fig. 3c matches the error graphs of [RLKV15, Figure 5,top-right] that were pointwise computed numerically.

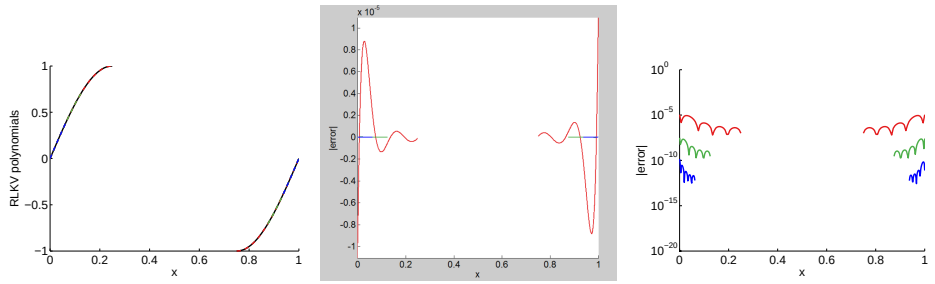

(a) RLKV-filtered polynomials (b) filtered - exact solution (c) Absolute error, log scale

FIG. 3. *RLKV-filtered boundary region of the DG output for d=3 of Example 2.3. The graphs in red, green, and blue correspond to i=1, 2, 3 respectively, i.e. to N=20, 40, 80 DG segments. (a) The three polynomials of degree 7 of the RLKV-filtered output with the exact solution (black dashed) superimposed. (b) The difference between the filtered output and the exact solution at very fine resolution. (c) Log scale of the absolute error left: $|P_{L,i}(x) - u_e(x)|$, $x \in [0, \lambda_{L,i}]$ and right: $|P_{R,i}(x) - u_e(x)|$, $x \in [\lambda_{R,i}, 1]$ at the computational resolution $6N$ (As (b) indicates, for higher resolution the arches would reach down to zero.)*

The polynomial characterization directly provides a symbolic expression for the derivatives of the convolved DG output.

Corollary 2.6 (Derivatives of PSIAC-filtered DG output [NP16]).

$$\frac{\mathrm{d}^\ell}{\mathrm{d}x^\ell}\big(u * f_x\big)(x) = \mathbf{u}_{\mathcal{I}}\, Q_\lambda\ \mathrm{diag}(h^{-(0:r)})\,\big(\frac{\mathrm{d}^\ell}{\mathrm{d}x^\ell}(x-h\lambda)^{0:r}\big)^t. \tag{2.14}$$

2.5. Boundary filters as PSIAC filters. The symmetric knot sequence of the symmetric kernel of degree d is

$$\mathbf{t} := h(-\mu, -\mu+1, \ldots, \mu), \quad \mu := \frac{r+d+1}{2},\ r := 2d. \tag{2.15}$$

On $[a..b]$, this symmetric kernel can only be applied at evaluation points x where

$$\lambda_{L,d} := a + \mu, \leq x \leq b - \mu =: \lambda_{R,d}. \tag{2.16}$$

The boundary SIAC kernels RS [RS03] and SRV [SRV11] of reproduction degree $r+1$ are of degree $k = d$, the degree of the DG output. Their index sequence $\mathcal{J}$ is consecutive, and they are defined over the shifted knots

$$\boldsymbol{t}_{*,d}(\xi) := \Big(-\mu, -\mu+1, \ldots, \mu\Big) + \xi - \lambda_{*,d}, \quad * \in \{L, R\} \tag{2.17}$$

that form a symmetric support about the origin when $\xi = \lambda_{*,d}$. The two kernels differ in their degree: $r(\mathrm{RS}) = 2d$ and $r(\mathrm{RV}) = 4d$. Explicit forms of the matrix G_λ, that is defined in Theorem 2.5 to efficiently construct the filter, are presented in [NP16].

The index sequence $\mathcal{J}$ of the boundary kernel RLKV [RLKV15] is non-consecutive. The left and right kernels are of degree $2d+1$ and are defined over the shifted knots, symmetric about the origin:

$$\boldsymbol{t}_{L,d}(\xi) := \Big(-\mu, \ldots, \mu-1, \underbrace{\mu, \ldots, \mu}_{d+1 \text{ times}} \Big) + \xi - \lambda_{L,d}, \tag{2.18}$$

$$\mathcal{J}_L := \{1 : (2d+1), 3d+1\};$$

$$\boldsymbol{t}_{R,d}(\xi) := \Big(\underbrace{-\mu, \ldots, -\mu}_{d+1 \text{ times}}, -\mu+1, \ldots, \mu, \Big) + \xi - \lambda_{R,d}, \tag{2.19}$$

$$\mathcal{J}_R := \{1, d : (3d+1)\}.$$

Explicit forms of the matrix G_λ, that is defined in Theorem 2.5 to efficiently construct the filter, are presented in [NP16].

Theorem 2.5 shows that a PSIAC filter need not have the same degree as the symmetric filter and it shows that PSIAC filters may have multiple knots without reducing the continuity of the filtered DG output. To illustrate this, [NP16] introduced filters with multiple interior knots. This class of filters is denoted NP_k and has knot sequences

$$\begin{aligned} \boldsymbol{t}_L &:= x - \lambda_L + \big(-\mu, \ldots, \mu-3, \mu-2, \underbrace{\mu-1, \cdots, \mu-1}_{k+1 \text{ times}}, \underbrace{\mu, \cdots, \mu}_{k+1 \text{ times}} \big), \\ \boldsymbol{t}_R &:= x - \lambda_R + \big(\underbrace{-\mu, \cdots, -\mu}_{k+1 \text{ times}}, \underbrace{-\mu+1, \cdots, -\mu+1}_{k+1 \text{ times}}, -\mu+2, -\mu+3 \ldots, \mu \big). \end{aligned} \tag{2.20}$$

3. New least-degree DG filters. The symbolic formulation (2.11) applies to kernels of degree different from the degree d of the DG output. We may therefore consider a piecewise-constant ($k = 0$) PSIAC filter. Notably, the NP_0 filter has a consecutive index sequence $\mathcal{J}$ and is defined over the shifted knots

$$\boldsymbol{t}_{*,d}(\xi) := \Big(-\mu, -\mu+1, \dots, \mu \Big) + \xi - \lambda_{*,d}, \quad \mu = \frac{3d+1}{2}, \quad * \in \{L, R\}. \tag{3.1}$$

The piecewise constant NP_0 filter has reproduction degree $r+1 = 3d+1$ and the same support size as the symmetric kernel. (Numerical experiments show that a filter with $2d+1$ constant pieces still achieves optimal superconvergence – albeit with a larger error than using $3d+1$ pieces. $3d+1$ is the number of pieces that the symmetric interior SIAC filter uses).

While the smoothness of the filtered output of position-*independent* filters, e.g. symmetric SIAC filters, depends on the filter degree, position-*dependent* PSIAC filters yield maximally smooth output regardless of their degree: by Theorem 2.5, the DG output filtered by a PSIAC filter is a polynomial over the respective boundary region independent of the degree or smoothness of the PSIAC filter. That is, even our piecewise constant NP_0 PSIAC filter increases the smoothness to infinity in the boundary region. Example 3.1 illustrates the remarkable fact that PSIAC filtering yields a single polynomial. This is in contrast to the finite smoothness at break points of data filtered with position-independent SIAC filters.

Example 3.1 (PSIAC-filtering yields polynomial output). *Let $h = 1$, $\chi_{[\alpha,\beta]}$ be the indicator function of $[\alpha, \beta]$ and*

$$u_{h_0}(x) := \chi_{[0,1]}(x) + \chi_{[3,4]}(x),\ x \in [0, 7] =: \Omega.$$

*the discontinuous DG output. Convolving $u_{h_0}(x)$ at x in the interior region $[2, 5]$ of Ω with the symmetric (position-*independent*) SIAC filter of reproduction degree $r = 1$,*

$$\mathcal{K}(s) := \frac{1}{2}B(s \,|\, -1 : 0) + \frac{1}{2}B(s \,|\, 0 : 1) = \frac{1}{2}\chi_{[-1,1]}(s),$$

yields

$$(\mathcal{K} * u_{h_0})(x) = \frac{1}{2}B(s \,|\, 2 : 4) + \frac{1}{2}B(s \,|\, 3 : 5), \quad x \in [2, 5]. \tag{3.2}$$

That is, convolving with $\mathcal{K}$ yields a C^0 output, as predicted by the SIAC theory developed by Ryan et al. [RS03, SRV11].

By contrast, at x in the left boundary region $[0, 2]$ of Ω, convolving $u_{h_0}(x)$ with the left-sided least-degree position-dependent PSIAC filter f_x defined in Example 2.2 yields

$$\begin{aligned}
\text{for } x \in [0,2]: \quad (f_x * u_{h_0})(x) &= \int_{\mathbb{R}} f_x(s) u_{h_0}(x-s)\mathrm{d}s \\
&\overset{\text{by Eq. (2.9)}}{=\!=\!=} f_{x;0} \int_{-2+x}^{-1+x} u_{h_0}(x-s)\mathrm{d}s + f_{x;1} \int_{-1+x}^{0+x} u_{h_0}(x-s)\mathrm{d}s \\
&\overset{0 \le x-s \le 2}{=\!=\!=} f_{x;0} \int_{-2+x}^{-1+x} \chi_{[0,1]}(x-s)\mathrm{d}s + f_{x;1} \int_{-1+x}^{0+x} \chi_{[0,1]}(x-s)\mathrm{d}s \\
&\overset{\text{change: } t = x-s}{=\!=\!=} f_{x;0} \int_1^2 \chi_{[0,1]}(t)\mathrm{d}t + f_{x;1} \int_0^1 \chi_{[0,1]}(t)\mathrm{d}t \\
&= f_{x;1} \overset{\text{by Eq. (2.10)}}{=\!=\!=} \frac{1}{2}(3-2x).
\end{aligned} \tag{3.3}$$

The equality Eq. (3.3) holds because when $0 \le x \le 2$ *and* $-2+x \le s \le 0+x$ *then* $0 \le x-s \le 2$. *Hence* $u_{h_0}(x-s) = \chi_{[0,1]}(x-s)$. *As Theorem 2.5 predicts* $(f_x * u_{h_0})(x) = \frac{1}{2}(3-2x)$, $x \in [0,2]$, *is a polynomial over the boundary region* $[0,2]$.

Fig. 4 graphs instances of the SRV, RLKV and NP_0 kernels. Note that the NP_0 filter remains piecewise constant, while the degree of the other two filters increases with the degree d of the DG data.

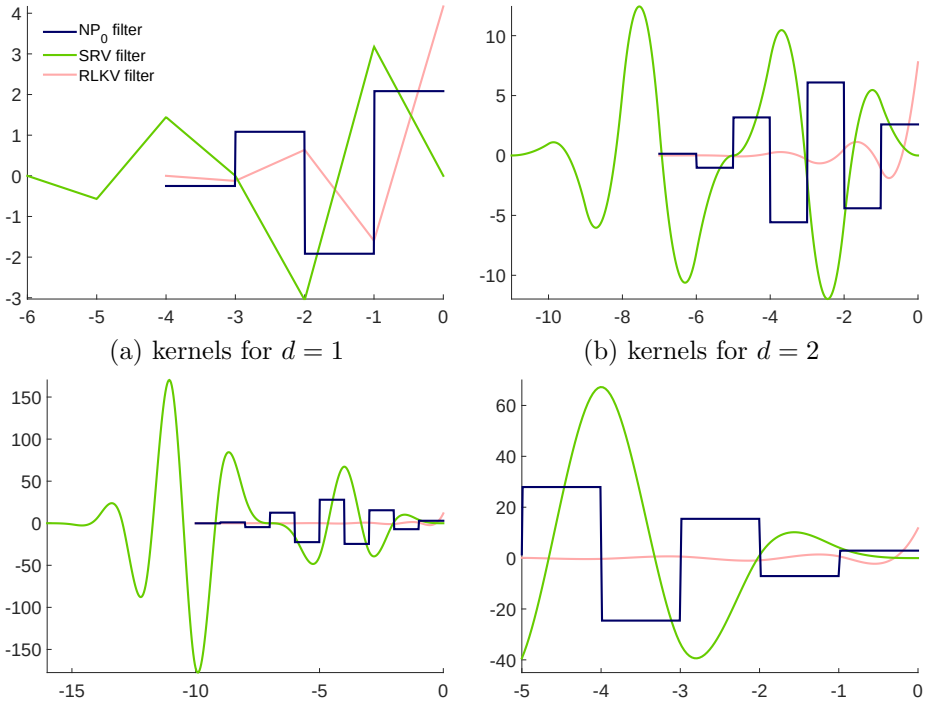

(a) kernels for $d = 1$ (b) kernels for $d = 2$

(c) kernels for $d = 3$ (c') right zoom of (c)

FIG. 4. *Graphs of the three kernels defined at the left boundary* $x = a$. *Note that the degree of [SRV11] and [RLKV15] increases with d while the degree of the new* NP_0 *kernel remains piecewise constant. The* NP_0 *kernel (blue) has the same support as the RLKV kernel (red), smaller than the SRV kernel (green).*

3.1. Symbolic form. We reduce the convolution of the DG data with the NP_0 kernels to an inner product of two short vectors. The inverse of the SIAC reproduction matrix $M_{\mathbf{t},\mathcal{J}}$ and the matrix G_{λ_*}, of the formulation (2.11) in Theorem 2.5, are explicitly derived for NP_0 based on the following two propositions.

PROPOSITION 3.1. *(SIAC reproduction matrix for degree* $k = 0$*) The SIAC reproduction matrix for least degree filters with index sequence* $\mathcal{J} := (0, \ldots, j_r)$ *and knot sequence* $t_{0:n}$ *is*

$$M_{t_{0:n},\mathcal{J}} = \left[\frac{t_{j+1}^{\delta+1} - t_j^{\delta+1}}{t_{j+1} - t_j}\right]_{\delta=0:r,\, j\in\mathcal{J}}. \tag{3.4}$$

If the knot sequence $t_{0:n}$ *is uniform, i.e.* $h_1 := t_{j+1} - t_j$, *then*

$$M_{t_{0:n},\mathcal{J}} = h_1^{-1}\left[(t_j + h_1)^{\delta+1} - t_j^{\delta+1}\right]_{\delta=0:r,\, j\in\mathcal{J}}. \tag{3.5}$$

Proof. Since $k = 0$, each entry of $M_{t_{0:n},\mathcal{J}}$ given by Eq. (2.6) is the sum of all monomials in t_{j+1} and t_j of total degree δ, and hence of the form (3.4). Eq. (3.5) is a direct consequence of Eq. (3.4). □

PROPOSITION 3.2 (G_{λ_*} for degree $k = 0$ and uniform DG intervals). *Assume that the DG break point sequence $s_{0:m}$ is uniform, hence after scaling consists of consecutive integers. Without loss of generality, the DG output on each interval $[s_i, s_{i+1}]$ is defined in terms of Bernstein-Bézier polynomials B^i_ℓ of degree d, where the superscript i indicates the interval and $\ell = 0 : d$, i.e.*

$$B^i_\ell(x) := \begin{cases} \binom{d}{\ell}(x - s_i)^\ell (s_{i+1} - x)^{d-\ell} & \text{if } x \in [s_i, s_{i+1}] \\ 0 & \text{otherwise.} \end{cases} \tag{3.6}$$

Let I be the $3d+1$ identity matrix and $\mathbf{1}$ the $(d+1)$ column vector of ones. The matrix G_{λ_L} for the left-sided kernel and the matrix G_{λ_R} for the right-sided kernel defined by Eq. (2.11) *are*

(3.7)

$$G_{\lambda_L} = G_{\lambda_R} = I \otimes \mathbf{1} = \frac{1}{d+1} \begin{bmatrix} 1 & \cdots & 1 & 0 & \cdots & 0 & \cdots & 0 & 0 & \cdots & 0 \\ 0 & \cdots & 0 & 1 & \cdots & 1 & \cdots & 0 & 0 & \cdots & 0 \\ \vdots & \ddots & \vdots & \vdots & \ddots & \vdots & \ddots & \vdots & \vdots & \ddots & \vdots \\ 0 & \cdots & 0 & 0 & \cdots & 0 & \cdots & 0 & 1 & \cdots & 1 \end{bmatrix}^t \in \mathbb{N}^{(d+1)(3d+1)} \times \mathbb{N}^{(3d+1)}.$$

Proof. First we derive Eq. (3.7) for G_{λ_L}. In Eq. (2.12), we change to the variable $t = s - \lambda_L + t_n$. Since the B-splines are translation invariant and $k = 0$ (hence $n = j_r + 1$)

$$B(s \,|\, \lambda - t_{n-j:j_r-j}) = B(t \,|\, t_n - t_{n-j:n-j-1}) = B(t \,|\, j : j+1). \tag{3.8}$$

Consequently, Eq. (2.12) can be rewritten as

$$G_{\lambda_L}(i,j) = \int_0^{3d+1} \phi_i(t\,;\, s_{0:m} - \lambda_L + t_n)\, B(t \,|\, j : j+1)\, \mathrm{d}t. \tag{3.9}$$

Since $s_0 = \frac{a}{h}$, the one-sided condition $\lambda_L = t_n + \frac{a}{h}$ implies that the first point of the sequence of translated DG break points $s_{0:m} - \lambda_L + t_n$ equals 0, i.e., $s_0 - \lambda_L + t_n = 0$. Since the break points are consecutive integers starting from 0 and the B-splines $B(t \,|\, j : j+1)$ are supported over $[0, 3d+1]$, the relevant DG break points are $0 : 3d+1$.

We re-write the basis functions $\phi_j(s\,;\, s_{0:m} - \lambda_L + t_n)$, that are supported on an interval $[i..i+1]$, in terms of DG output Bernstein-Bézier basis functions B^i_ℓ, $\ell = 0..d$. Since each B-spline $B(t \,|\, j : j+1)$ is supported on $[j, j+1]$ and each B^i_ℓ is supported on $[i, i+1]$, the entries of G_{λ_L} are non-trivial only if $i = j$. Therefore

$$G_{\lambda_L}\big((d+1)i + \ell, i\big) = \int_i^{i+1} B^i_\ell(t)\, B(t \,|\, i : i+1)\, \mathrm{d}t = \frac{1}{h} \times \frac{h}{d+1} = \frac{1}{d+1}. \tag{3.10}$$

The second last equality in Eq. (3.10) holds since $B(t \,|\, i : i+1)|_{[i,i+1]} \equiv \frac{1}{h}$ and the integral of $B^i_\ell(t)$ over $[i, i+1]$ equals $\frac{h}{d+1}$ [dB02]. Eq. (3.10) shares the entries of Eq. (3.7) for G_{λ_L}.

A similar argument for deriving G_{λ_R} but starting with the substitution $t := -(s - \lambda_R + t_0)$ proves Eq. (3.7) for G_{λ_R}. □

3.2. Filter transition. Let $\mathcal{L}_x * u_h$ denote the DG output u_h filtered by the left boundary PSIAC filter $\mathcal{L}_x$ and $\mathcal{K} * u_h$ the DG output filtered by the symmetric interior filter $\mathcal{K}$. These two filtered outputs overlap on the interval $[a_1, a_2] = a + c_L + [0..2h]$ where c_L separates the interior and left boundary. Without loss of generality, after substituting $z := (x - a_1)/(a_2 - a_1)$, we may assume that $a_1 := 0$, $a_2 := 1$. [SRV11] suggests a smoothness-preserving transition filtering scheme that we state more succinctly as

$$u_h^\star(x) := (1 - \alpha(x)) \left(\mathcal{L}_x * u_h\right)(x) + \alpha(x) \left(\mathcal{K} * u_h\right)(x), \tag{3.11}$$
$$\alpha(x) := \sum_{i=0}^{2\rho} \alpha_i B_i(x), \quad \alpha_i := \begin{cases} 0 & \text{if } i \leq \rho; \\ 1 & \text{else.} \end{cases}$$

where $B_i(x) = \binom{2\rho}{i}(1-x)^{2\rho-i}x^i$ are Bernstein-Bézier polynomials of degree 2ρ defined over the unit interval $[0..1]$. The Bernstein-Bézier representation guarantees that $u_h^\star$ Hermite-interpolates both filtered DG output up to order ρ. The degree 2ρ need not be twice the minimum degree of the boundary filter and the symmetric filter but can be chosen to further smooth out the transition. That is, one may choose $\rho = 2$ even though $d = k = d_s = 1$. The transition for $\rho = 2$ is less abrupt at 0 and 1 than for $\rho = 1$.

4. Numerical Comparison of the SRV, RLKV, NP_0 and the symmetric SIAC filter. The goal of this section is to compare the new NP_0 filters with the state-of-the-art filters, SRV [SRV11] and RLKV [RLKV15] in their stable symbolic form [NP16]. In particular, this section explains and discusses the graphs in the Appendix that represent ca. 15000 convergence rate measurements. All errors are computed on the regions where the filters apply. That is, the error of the boundary filters is measured on the boundary regions only, the error of the symmetric SIAC filter is measured only in the interior, whereas the error of the DG output is measured over the whole domain.

The comparison will be based on three test problems that are special instances of the canonical problem (2.2), $\frac{du}{d\tau} + \frac{d}{dx}\Big(\kappa(x,\tau)\, u\Big) = \rho(x,\tau)$ for $x \in (a..b)$, $\tau \in (0..T)$. That is, we measure the convergence not just for the final time $T = 2\pi$ but also for many other final times such as $T = 0.7 * 2\pi$.

Test 4.1 (Constant wave-speed, *periodic* boundary conditions). *Consider the specializations of Eq.* (2.2)*:*

$$\kappa(x,\tau) \equiv 1, \quad \rho(x,\tau) \equiv 0, \quad 0 \leq \tau \leq T, \tag{4.1}$$

$a := 0$, $b := 1$, periodic boundary conditions, $u_0(x) := \sin(2\pi x)$. The exact solution at the final time T is $u(x,T) = \sin(2\pi(x - T))$.

Test 4.2 (Constant wave-speed, *Dirichlet* boundary conditions). *Consider Eq.* (2.2) *with specializations* (4.1)*, but $a := 0$, $b := 2\pi$, Dirichlet boundary conditions, $u_0(x) := \sin(x)$, $u(0,\tau) := -\sin(\tau)$. The exact solution is at the final time T is $u(x,T) = \sin(x - T)$.*

Test 4.3 (*Variable* wave-speed, periodic boundary conditions). *Consider Eq.* (2.2) *with the specializations*

$$\kappa(x,\tau) := 2 + \sin(x + \tau), \quad \rho(x,\tau) := \cos(x - \tau) + \sin(2x), \quad 0 \leq \tau \leq T, \tag{4.2}$$

$a := 0$, $b := 2\pi$, and periodic boundary conditions, $u_0(x) := \sin(x)$. The exact solution at the final time T is $u(x,T) = \sin(x - T)$.

The comparison of the filters yields broadly the same qualitative results for all three test scenarios. We display the L^∞ and the L^2 convergence rates in the Appendix but discuss the results in this section.

Fig. 7, 8 and 9 juxtapose the *maximal point-wise errors for each final time* T of the DG output (over the whole domain) with that of the boundary filters SRV, RLKV, NP_0 (restricted to the boundary regions) and the symmetric SIAC filter (restricted to the interior). The symmetric SIAC filter is graphed as a light grey dotted line and applies and always yields the optimal convergence rate $2d+1$. This **time series** of errors differs from the commonly-used error graphs such as in Fig. 1a,b,c, where the abscissa represents the one-dimensional domain of computation for a fixed T. By contrast in Fig. 7, 8 and 9 the abscissa represents the final time T for computing the Test equation. That is, $T = 0.4$ means that the equations has been computed by DG up to time $T = 0.4$ (rather than $T = 1$) and then the filters have been applied. The graphs therefore represent a large number of measurements: for each final time T on the abscissa, for each boundary filter, the ordinates of Fig. 7, 8 and 9 show the maximal point-wise error over the region where they apply.

Fig. 10, 11 and Fig. 12 display a final-time series of the convergence rates

$$\rho = \rho(\tau, h) := \ln\big(\frac{\text{error at time } \tau \text{ for mesh size } 2h}{\text{error at time } \tau \text{ for mesh size } h}\big)/\ln 2. \tag{4.3}$$

for the L^2 and the L^∞ norm, and for the left boundary region and the right boundary region. Fig. 10 and Fig. 11 each show #(degrees×norms×boundary regions×final times×filter types & DG output ×refinements) = (3×2×2×50×5×2) = 6000 convergence rates. Fig. 12, with 30 final times, shows 3600 convergence rates. For example, in Fig. 5a, at final time $T = 0.3$, the convergence rate for symmetric SIAC filter (restricted to the interior of the domain) for degree $k = 1$ is $\rho = 3$; the rate for the RLKV-filter (restricted to the boundary regions) is $\rho = 2$; and the rates are $\rho = 3$ for the SRV-filter and the NP_0-filter.

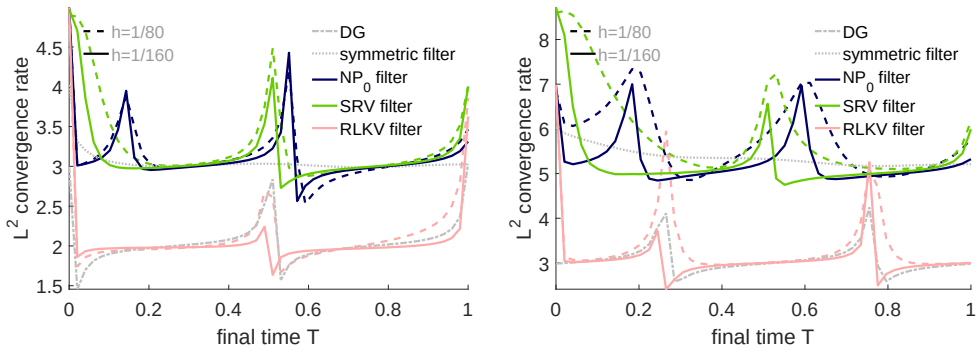

(a) $d = k = 1$ ($k = 0$ for the NP_0 filter) (b) $d = k = 2$ ($k = 0$ for the NP_0 filter)

FIG. 5. **Convergence rate time series** *Test 4.1 (constant wave-speed, periodic boundary condition) for L^2-error convergence rates of PSIAC filters. Each point on the abscissa represents one final time $0 \le T \le 1$ and each ordinate represents a L^2-convergence rate. A complete set of graphs is shown in Fig. 10.*

The time-series yields additional insights: The convergence rate fluctuates with T and can be particularly high for some specific final times T. And the time series in

the Dirichlet scenario in Fig. 6 shows spikes in the error, for all filters including the symmetric SIAC filters.

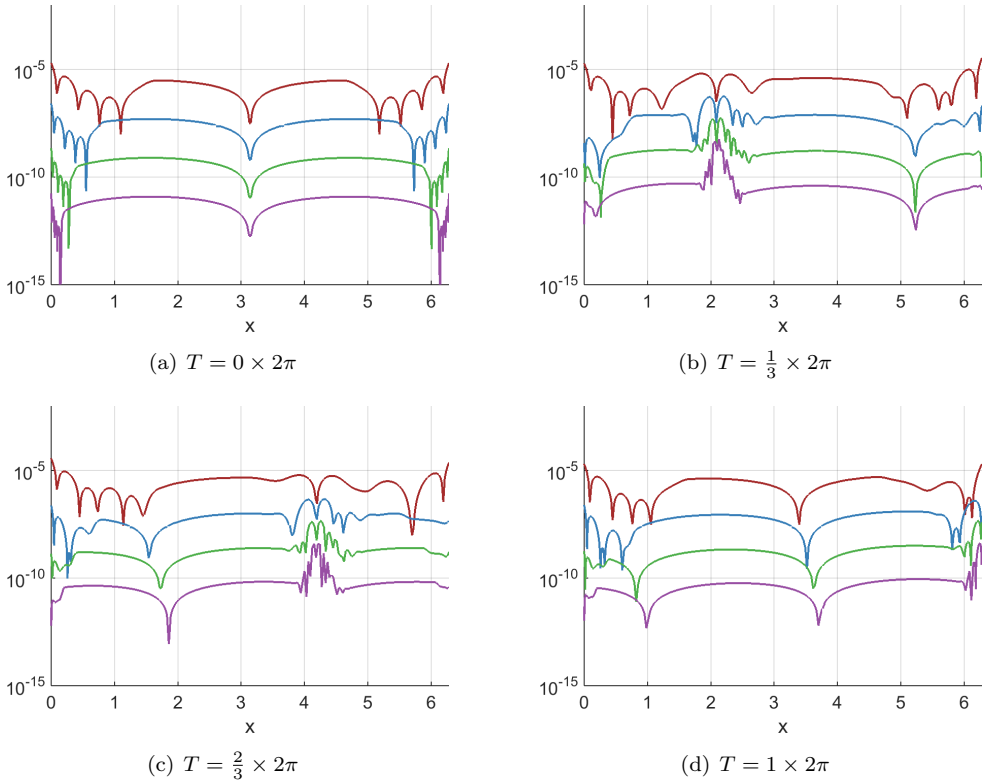

(a) $T = 0 \times 2\pi$ (b) $T = \frac{1}{3} \times 2\pi$

(c) $T = \frac{2}{3} \times 2\pi$ (d) $T = 1 \times 2\pi$

FIG. 6. *Travelling spikes the in pointwise error graphs of the filtered degree $d = 2$ DG output. for the Dirichlet problem 4.2. The pointwise errors are for mesh-size $h = 20^{-1}, 40^{-1}, 80^{-1}, 160^{-1}$ (drawn in red, blue, green, purple respectively and from top to bottom in each panel)*

Fig. 7 confirms, for all final times, the lower error of the SRV filter compared to the RLKV filter. However, instability of the SRV filter at double precision for certain final times T and higher degree of the DG output increase the error, even above that of the raw DG output (see Fig. 8 for $d = 2, 3$ and Fig. 9 for $d = 3$). Similarly, instability causes the error of SRV to exceed that of the NP_0 filter. Overall, when $d = 1$ or $d = 2$, point-wise errors of the RLKV filter are noticeably larger than those of the SRV filter and the NP_0 filter. The point-wise errors of the NP_0 filter are on par with the symmetric SIAC filter (in gray).

We note the consistency between L^2 and L^∞ convergence and therefore clearly higher rates for SRV, NP_0 and the symmetric filters over RLKV. When $d = 1$ and $d = 2$, the NP_0 and SRV filters show optimal L^2 and L^∞ super-convergence rates of order $2d+1$. The convergence rate two for the boundary regions for RLKV and $d = 1$ has been verified also with the original RLKV code.

For $d = 3$ the point-wise errors and convergence rates of all filters oscillate when the calculations are close to machine precision. However, the point-wise errors and convergence rates of the NP_0 filter are on par with that of the symmetric SIAC filter, while the errors of the SRV filters are notably higher and convergence rates become

sub-optimal, and even lower than $d+1$ for some T when $d=3$.

Fig. 2 helps explain the instability of the SRV filters. Plotting the alternating entries of the convolution vector $\boldsymbol{\mathcal{V}} = Q_\lambda \boldsymbol{\lambda}$ at a boundary point x (e.g., $x=0$ when $a=0$), we find the entries of the SRV filters to be two orders of magnitude larger than those of NP_0.

5. Conclusion. The newly-discovered PSIAC NP_0 filters possess three main advantages, especially when combined with the symmetric SIAC filter in the interior. First, the computation of the NP_0 filters and their application for convolution is more stable due to their explicit representation as small integer fractions. Second, on canonical test equations, applying NP_0 filters reduces the errors of the DG output to that of optimal symmetric SIAC filters. Third, support of the NP_0 filters are of the same size as those of the symmetric SIAC filters making them naturally compatible.

Acknowledgement. This work was supported in part by NSF grant CCF-1117695 and NIH grant R01 LM011300-01. Jennifer Ryan kindly provided her group's RLKV-code to allow us to confirm correctness of our symbolic implementation of RLKV.

REFERENCES

[BS77] J.H. Bramble and A.H. Schatz. Higher order local accuracy by averaging in the finite element method. *Math Comput*, 31(137):94–111, January 1977.

[CLSS03] B. Cockburn, M. l. Luskin, C.-W. Shu, and E. Süli. Enhanced accuracy by post-processing for finite element methods for hyperbolic equations. *Math Comput*, 72(242):577–606, 2003.

[dB02] C.W. de Boor. B-spline Basics. In M. Kim G. Farin, J. Hoschek, editor, *Handbook of Computer Aided Geometric Design*. Elsevier, 2002.

[dB05] C. W. de Boor. Divided differences. *Surveys in Approximation Theory*, 1:46–69, 2005.

[HW07] J.S. Hesthaven and T. Warburton. *Nodal Discontinuous Galerkin methods: algorithms, analysis, and applications*. Springer Science & Business Media, 2007.

[JVSRV14] Liangyue Ji, Paulien Van Slingerland, Jennifer Ryan, and Kees Vuik. Superconvergent error estimates for position-dependent smoothness-increasing accuracy-conserving (SIAC) post-processing of Discontinuous Galerkin solutions. *Math Comput*, 83(289):2239–2262, 2014.

[LRKV16] X. Li, J.K. Ryan, R.M. Kirby, and C. Vuik. Smoothness-increasing accuracy-conserving (SIAC) filters for derivative approximations of Discontinuous Galerkin (DG) solutions over nonuniform meshes and near boundaries. *J Comput Appl Math*, 294:275 – 296, 2016.

[ML78] M.S. Mock and P.D. Lax. The computation of discontinuous solutions of linear hyperbolic equations. *Commun Pur Appl Math*, 31(4):423–430, 1978.

[MRK12] H. Mirzaee, J.K. Ryan, and R. M. Kirby. Efficient implementation of smoothness-increasing accuracy-conserving (SIAC) filters for Discontinuous Galerkin solutions. *SIAM J Sci Comput*, 52(1):85–112, 2012.

[MRK15] M. Mirzargar, J.K. Ryan, and R.M. Kirby. Smoothness-increasing accuracy-conserving (SIAC) filtering and quasi-interpolation: A unified view. *SIAM J Sci Comput*, pages 1–25, 2015.

[NP16] D.-M. Nguyen and J. Peters. Non-uniform Discontinuous Galerkin Filters via Shift and Scale. *SIAM Journal on Numerical Analysis, to appear*, 2016.

[Pet15] J. Peters. General spline filters for Discontinuous Galerkin solutions. *Comp Math Appl*, 70(5):1046 – 1050, 2015.

[RC09] J.K. Ryan and B. Cockburn. Local derivative post-processing for the Discontinuous Galerkin method. *J Comput Phys*, 228(23):8642 – 8664, 2009.

[RLKV15] J.K. Ryan, X. Li, R.M. Kirby, and K. Vuik. One-sided position-dependent smoothness-increasing accuracy-conserving (SIAC) filtering over uniform and non-uniform meshes. *SIAM J Sci Comput*, 64(3):773–817, 2015.

[RS03] J.K. Ryan and C.-W. Shu. On a one-sided post-processing technique for the Discon-

tinuous Galerkin methods. *Methods and Applications of Analysis*, 10(2):295–308, 2003.

[RSA05] J.K. Ryan, C.-W. Shu, and H. Atkins. Extension of a post processing technique for the Discontinuous Galerkin method for hyperbolic equations with application to an aeroacoustic problem. *SIAM J Sci Comput*, 26(3):821–843, 2005.

[SRV11] P.v. Slingerland, J.K. Ryan, and C. Vuik. Position-dependent smoothness-increasing accuracy-conserving (SIAC) filtering for improving Discontinuous Galerkin solutions. *SIAM J Sci Comput*, 33(2):802–825, 2011.

[Tho77] V. Thomée. High order local approximations to derivatives in the finite element method. *Math Comput*, 31(139):652–660, 1977.

Appendix: Numerical experiments - Error Graphs and Convergence Rates. The following graphs compare the maximal pointwise errors and convergence rates for the filtered DG output. The DG output is of degree $d = 1, 2, 3$ with a uniform partition of the x-domain into intervals of length $h = 1/N$ and $N = 20, 40, 80, 160$. Independent of N, a fixed number points in the boundary regions are the result of filtering with (the symbolic version of) SRV, RLKV, or by NP_0. Boundary filters are measured only in the boundary regions inclusive of the transition region and errors of the symmetric filter are computed only for the interior exclusive of the transition region. Under refinement the interior converges to the full domain and for uniformly-spaced DG output the symmetric SIAC filter contributes an increasing number of values, while the number of values from the boundary filter remains the same. Computing the L^2 error over the full domain, say $[0..2\pi]$, does not assess boundary filters correctly since the error is dominated by the error of the increasing number of symmetric-filtered samples. Consequently, errors and rates for the boundary filters are *not combined* with those of the symmetric filter. (For all cases presented, the combined or global L^2 error is that of the symmetric SIAC filter.)

Unlike Fig. 1, the graphs do *not* show errors at domain points x at a fixed time T. Rather the errors are plotted as functions of final time T, i.e. as a ***final-time series***. Each plot for Test 4.1 and Test 4.2 shows the errors at $N = 50$ uniformly-spaced final times T in $[0, 1]$ and $[0, 2\pi]$ respectively. Those for Test 4.3 correspond to $N = 30$ uniformly-spaced T in $[0, 2\pi]$. That is, the graphs summarize the error measurements for each final time T. For example, the value of the RLKV error graph at final time $T = 0.4$ corresponds to solving the indicated Test equation by DG up to time $T = 0.4$, then convolving with RLKV at the boundary and computing the error of the fixed number of RLKV-filtered samples, e.g. 18 samples for $d = 1$ and six samples per interval. When $N = 40$ the error of the symmetric SIAC filter is then computed at $N - 18$ points. The samples within each of the N intervals ar uniformly distributed. Changing the sample points to Gauss-Legendre points does not change the picture.

All graphs share the same color and style assignments. The raw *DG* output time series is graphed in light grey. In Fig. 7, 8, and 9, the raw *DG* output time series is typically the top-most graph (largest error) and the bottom-most in the graphs of Fig. 10, 11 and 12 that show the convergence-rate. The symmetric SIAC filter for the given degree is graphed in light grey, typically located in the middle and relatively straight. The symmetric SIAC filter only applies in the interior: for the different final times, the maximal pointwise error, respectively the convergence rate over the domain interior is plotted. The boundary filters are RLKV (red), SRV(green) and NP_0 filter (blue). In subfigures (a), (b), (c), (d), *dashed graphs* correspond to $N = 80$ and *solid graphs* to $N = 160$, a halving of h. For (e) and (f) In subfigures (e) and (f) *dashed graphs* correspond to $N = 40$ and *solid graphs* to $N = 80$.

Fig. 10 for Test 4.1 and Fig. 11 for Test 4.2, and Fig. 12 for Test 4.3 display the

L^∞ and L^2 convergence rates of the filtered DG outputs obtained after convolving with the filters (symmetric SIAC in the interior – SRV, RLKV or NP_0 in the boundary region). All computations are performed in double precision.

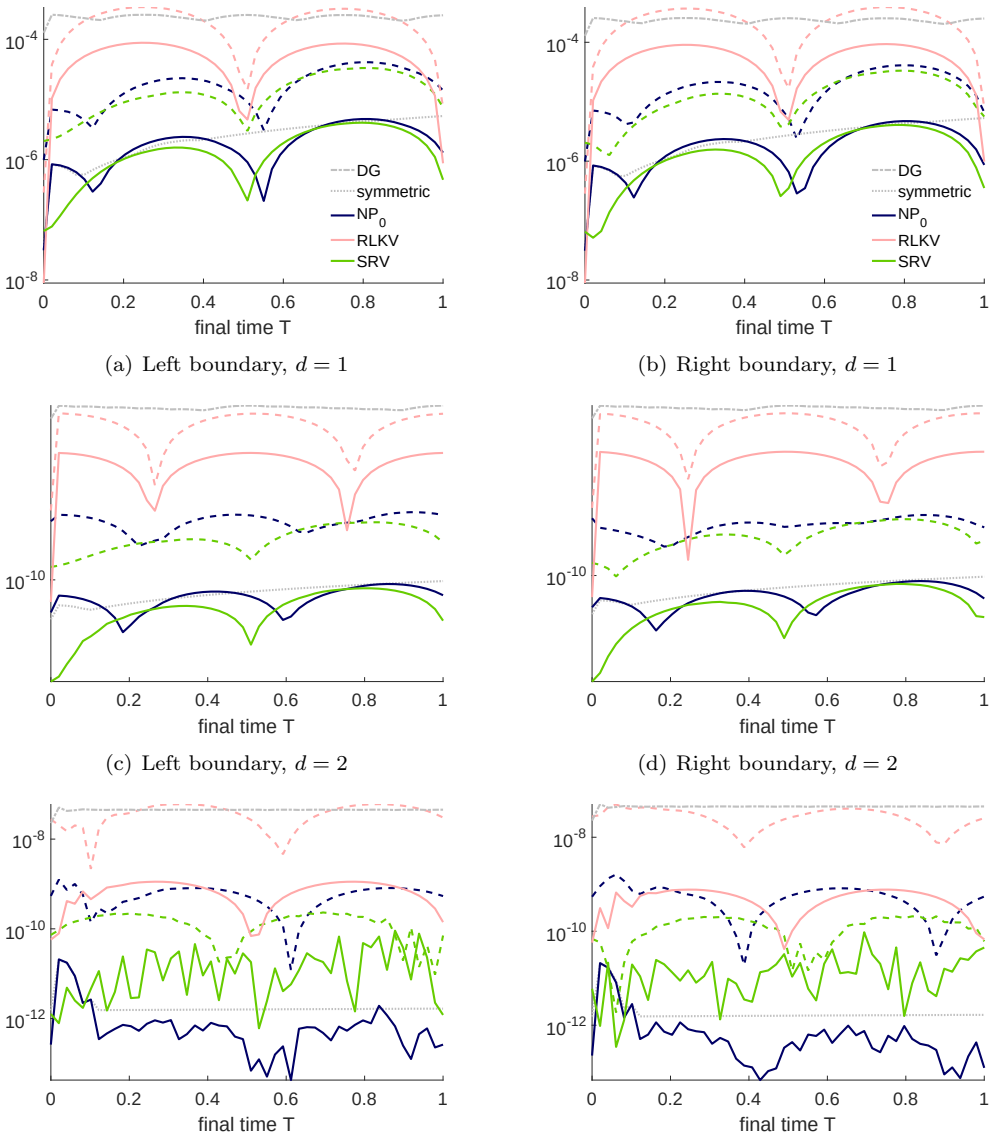

(a) Left boundary, $d = 1$

(b) Right boundary, $d = 1$

(c) Left boundary, $d = 2$

(d) Right boundary, $d = 2$

(e) Left boundary, $d = 3$

(f) Right boundary; $d = 3$

FIG. 7. ***Error*** *Test 4.1 (constant wave-speed, periodic boundary condition). Abscissa: final time T at which the DG output is computed; ordinate: maximum point-wise errors of filtered DG data; Dashed graphs correspond to $N = 80$ in (a), (b), (c), (d) and to $N = 40$ in (e), (f). Solid graphs correspond to $N = 160$ in (a), (b), (c), (d) and to $N = 80$ in (e), (f).*

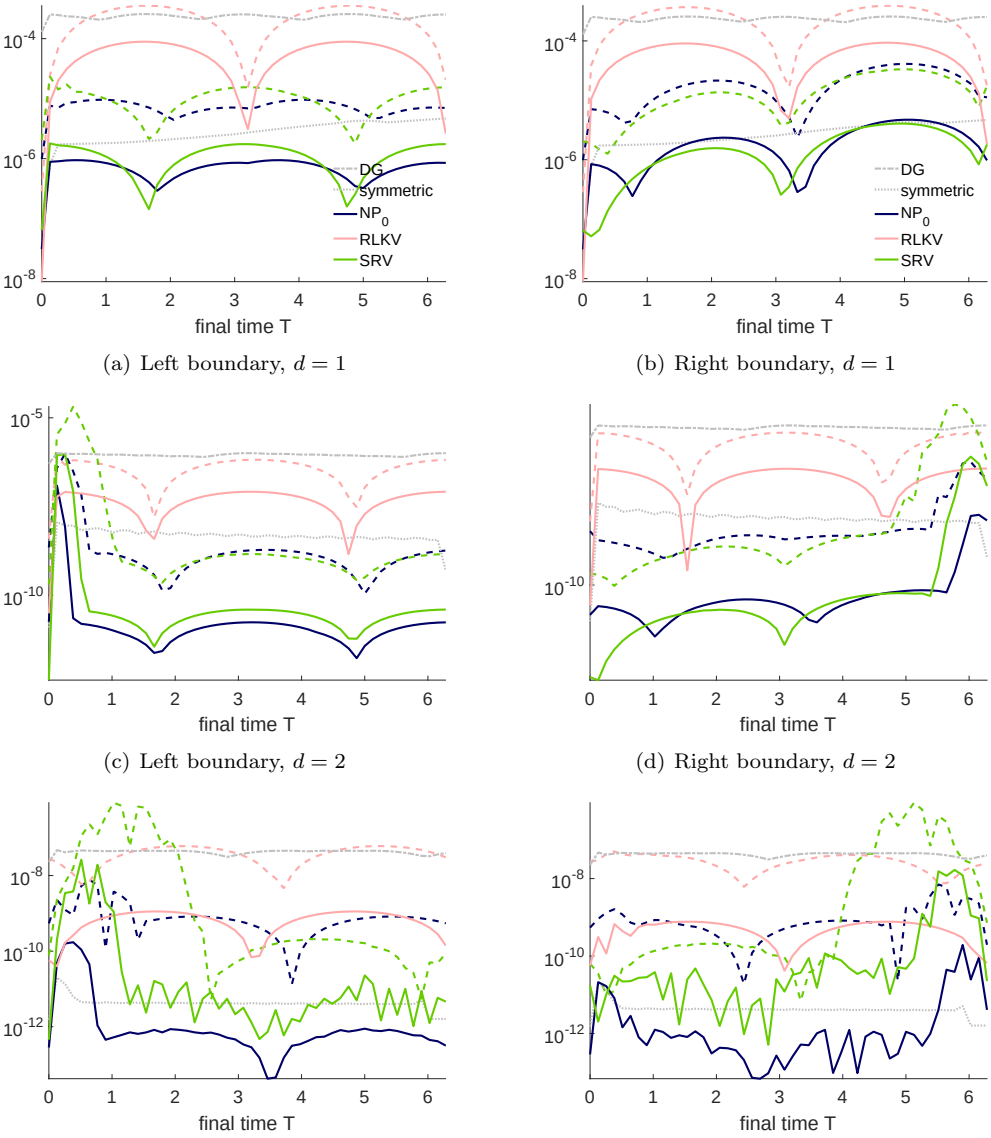

(a) Left boundary, $d = 1$

(b) Right boundary, $d = 1$

(c) Left boundary, $d = 2$

(d) Right boundary, $d = 2$

(e) Left boundary, $d = 3$

(f) Right boundary; $d = 3$

FIG. 8. ***Error*** *Test 4.2 (constant wave-speed, Dirichlet boundary condition). Abscissa: final time T at which the DG output is computed; ordinate: maximum point-wise errors of filtered DG data; Dashed graphs correspond to $N = 80$ in (a), (b), (c), (d) and to $N = 40$ in (e), (f). Solid graphs correspond to $N = 160$ in (a), (b), (c), (d) and to $N = 80$ in (e), (f).*

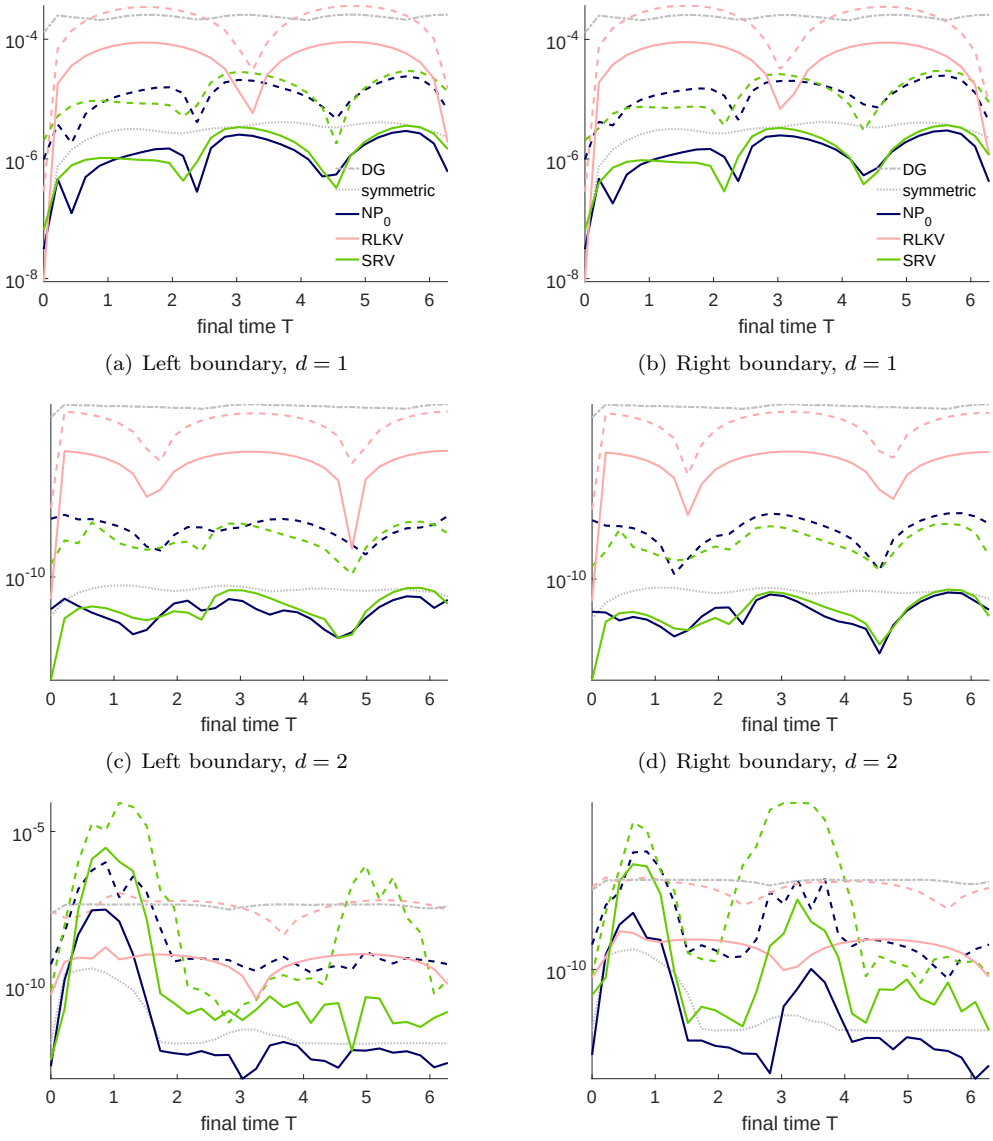

(a) Left boundary, $d = 1$

(b) Right boundary, $d = 1$

(c) Left boundary, $d = 2$

(d) Right boundary, $d = 2$

(e) Left boundary, $d = 3$

(f) Right boundary; $d = 3$

FIG. 9. ***Error*** *Test 4.3 (variable wave-speed, periodic boundary condition). Abscissa: final time T at which the DG output is computed; ordinate: maximum point-wise errors of filtered DG data; Dashed graphs correspond to $N = 80$ in (a), (b), (c), (d) and to $N = 40$ in (e), (f). Solid graphs correspond to $N = 160$ in (a), (b), (c), (d) and to $N = 80$ in (e), (f).*

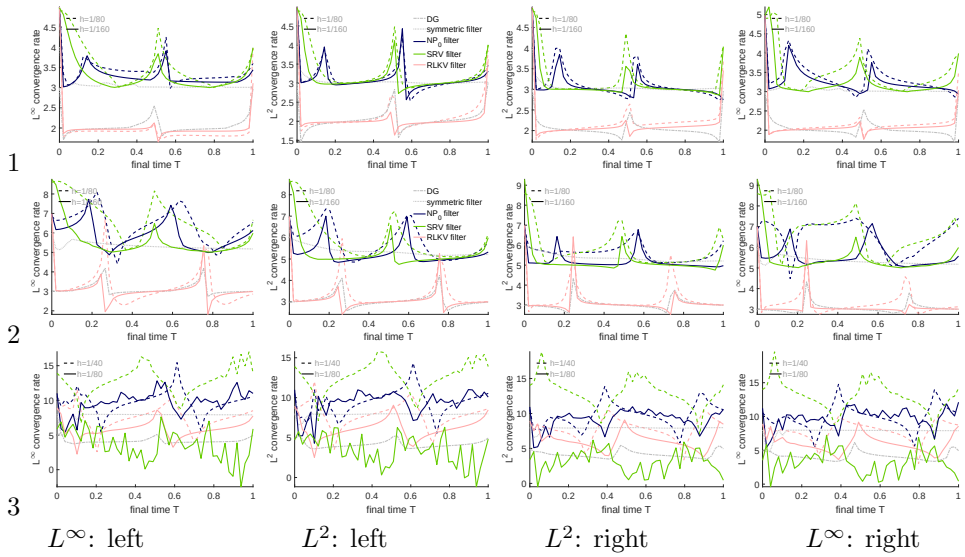

FIG. 10. ***Convergence rates*** *Test 4.1 (constant wave-speed, periodic boundary condition). L^2- and L^∞ convergence rates of the convolved DG data at left and right boundary. Rows $1, 2, 3$ show rates for degree $d = 1, 2, 3$. The graphs have the same indicative colors and styles as those in Fig. 7, 8 and 9.*

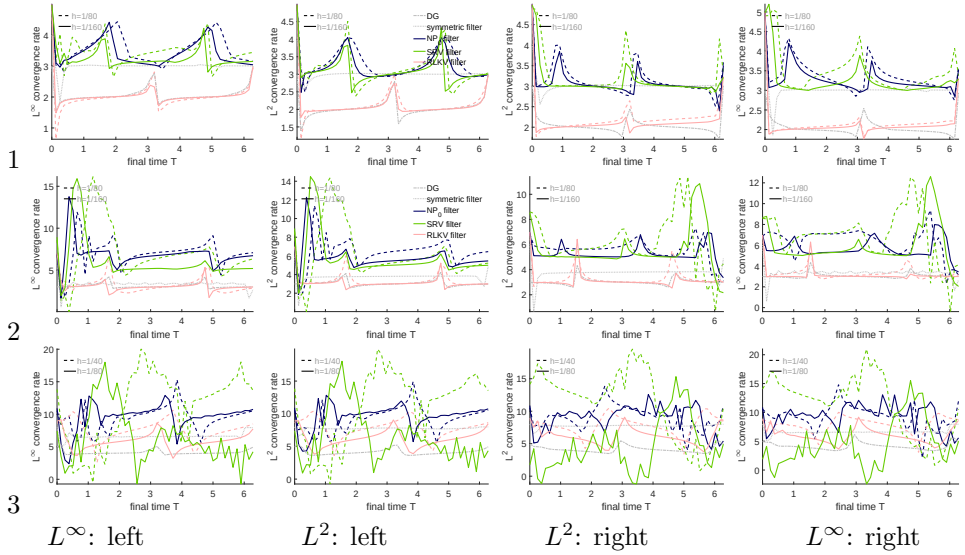

FIG. 11. ***Convergence rates*** *Test 4.2 (constant wave-speed, Dirichlet boundary condition). L^2- and L^∞ convergence rates of the convolved DG data at left and right boundary. Rows $1, 2, 3$ show rates for degree $d = 1, 2, 3$.*

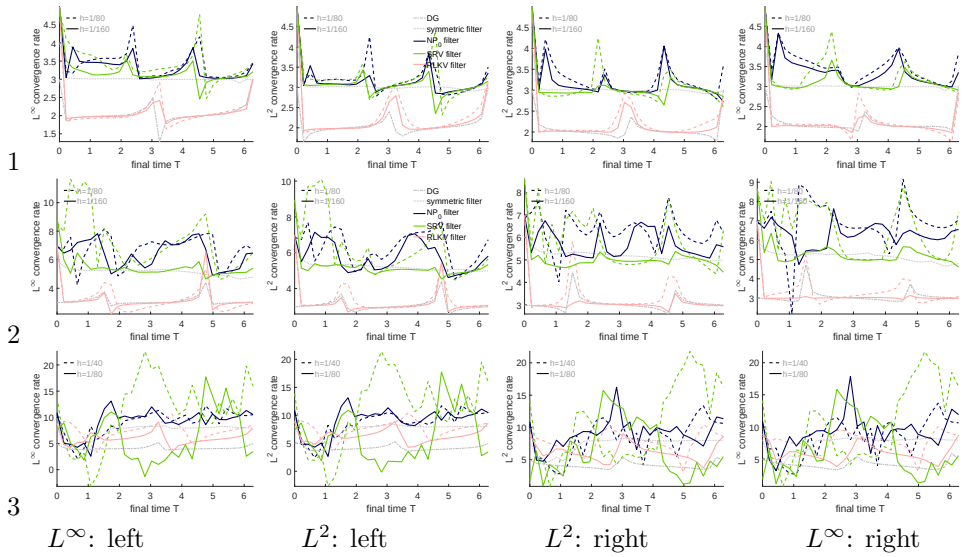

FIG. 12. ***Convergence rates*** *Test 4.3 (variable wave-speed, periodic boundary condition). L^2- and L^∞ convergence rates of the convolved DG data at left and right boundary. Rows $1, 2, 3$ show rates for degree $d = 1, 2, 3$.*